Rare Metal Materials and Engineering
Volume 55, Issue 3, March 2026
Available online at www.rmme.ac.cn

Science Press

Cite this article as: Chen Xia, Zhu Yulong, Liu Quanyi, et al. Hot Compression Deformation Behavior and Processing Maps of Mg-Zn-Mn(-Sn)-Ca Alloy[J]. Rare Metal Materials and Engineering, 2026, 55(03): 627-635. DOI: https://doi.org/10.12442/j.issn.1002-185X.20250156.

ARTICLE

Hot Compression Deformation Behavior and Processing Maps of Mg-Zn-Mn(-Sn)-Ca Alloy

Chen Xia[1], Zhu Yulong[1], Liu Quanyi[1], Zhang Dingfei[2], Pan Fusheng[2]

[1] College of Civil Aviation Safety Engineering, Civil Aviation Flight University of China, Guanghan 618307, China; [2] College of Materials Science and Engineering, Chongqing University, Chongqing 400045, China

Abstract: The hot compression deformation behavior of Mg-6Zn-1Mn-0.5Ca (ZM61-0.5Ca) and Mg-6Zn-1Mn-2Sn-0.5Ca (ZMT612-0.5Ca) alloys was investigated at deformation temperatures ranging from 250 ℃ to 400 ℃ and strain rates varying from 0.001 s^{-1} to 1 s^{-1}. The results show that the addition of Sn promotes dynamic recrystallization (DRX), and CaMgSn phases can act as nucleation sites during the compression deformation. Flow stress increases with increasing the strain rate and decreasing the temperature. Both the ZM61-0.5Ca and ZMT612-0.5Ca alloys exhibit obvious DRX characteristics. CaMgSn phases can effectively inhibit dislocation motion with the addition of Sn, thus increasing the peak flow stress of the alloy. The addition of Sn increases the hot deformation activation energy of the ZM61-0.5Ca alloy from 199.654 kJ/mol to 276.649 kJ/mol, thus improving the thermal stability of the alloy. For the ZMT612-0.5Ca alloy, the optimal hot deformation parameters are determined to be a deformation temperature range of 350–400 ℃ and a strain rate range of 0.001–0.01 s^{-1}.

Key words: hot deformation; constitutive equation; processing map; deformation activation energy; magnesium alloy

1 Introduction

Magnesium (Mg) alloys, as one the lightest structural metallic materials, have great application potential in the automobile, aerospace, and electronics industries. This is primarily attributed to their low density, high specific strength and stiffness, excellent magnetic shielding ability, and good damping ability[1–3]. Among wrought Mg alloys, Mg-Zn alloys are typical high-strength representatives; they have attracted increasing attention because of their substantial solid-solution strengthening and significant precipitation hardening effects[4–6]. However, Mg alloys still suffer from relatively low strength, compared with competing materials (i.e. aluminum alloys and steels), which remains the main reason restricting their extensive industrial application. To further improve the mechanical properties of Mg-Zn alloys, many efforts have been devoted, such as alloying is a key strategy. Rare earth (RE) elements are the most commonly used alloying additions for this purpose, but the high cost of RE metals restricts their large-scale application. Thus, it is necessary to develop new Mg alloys either via microalloying or by completely replacing RE elements with some low-cost alternative elements.

Calcium (Ca) is considered as a highly attractive alloying element because of its low cost. Du et al[7–8] discovered that alloying Mg-6Zn alloys with Ca enhances the strength of the extruded products. Zhang et al[9] reported that adding Ca to extruded Mg-Zn alloys not only weakens the strong basal texture but also refines the grain size. Tin (Sn) is another alloying element which can significantly reduce the critical resolved shear stress (CRSS) of pyramidal slip, hence contributing to improved plastic deformation capacity[5]. In the Mg-Sn-Ca alloy system, the formed CaMgSn phase presents a strip-like morphology and exerts a more effective pinning effect on the grain boundary, which helps to refine the microstructure[10–12]. In our previous studies, we found that the addition of 2wt% Sn significantly enhances the mechanical properties of as-extruded and peak-aged Mg-6Zn-1Mn-0.5Ca (ZM61-0.5Ca) alloys[13–14].

Received date: March 26, 2025
Foundation item: Sichuan Science and Technology Program (2025ZNSFSC1341); Fundamental Research Funds for the Central Universities (J2022-090, 25CAFUC04087)
Corresponding author: Chen Xia, Ph. D., College of Civil Aviation Safety Engineering, Civil Aviation Flight University of China, Guanghan 618307, P. R. China, E-mail: chenxia13091025@163.com

However, with the increase in alloying element content, several issues may arise, such as casting defects, the formation of precipitates (along with their non-uniform distribution and morphology), micropores, and chemical segregation[15]. To address these issues, thermomechanical processing of the alloy at higher temperatures is required. Previous studies mainly focused on the microstructure and mechanical properties of Mg-Zn-Sn-Ca alloys, but relatively few studies have been conducted on their hot deformation behavior. Therefore, the present study is mainly focused on the hot deformation behavior of Mg-6Zn-1Mn-*x*Sn-0.5Ca (*x*=0, 2) alloy.

In this study, therefore, the plastic flow behavior of ZM61-0.5Ca and Mg-6Zn-1Mn-2Sn-0.5Ca (ZMT612-0.5Ca) magnesium alloys under different deformation conditions were investigated. In addition, the processing maps of ZM61-0.5Ca and ZMT612-0.5Ca alloys at different strain levels were constructed to determine the optimum conditions for hot working process.

2 Experiment

Cast ingots of the experimental alloys were prepared using commercial-purity Mg (>99.9wt%), high-purity Zn (>99.95wt%), high-purity Sn (>99.9wt%), as well as Mg-2.7Mn and Mg-12Ca master alloys. After removing surface oxides from the raw materials, all alloys were melted at about 720 ℃ in a vacuum furnace (ZG-0.0) under argon gas protection. The chemical composition of the experimental alloy ingots was analyzed by an XRF-800 CCDE X-ray fluorescence spectrometer, and the results are given in Table 1. The ingots were then homogenized at 330 ℃ for 14 h, followed by heating to 420 ℃ and holding for 2 h. Then, the homogenized ingots were machined into cylindrical samples with dimensions of *Φ*8 mm×12 mm for hot compression tests, as shown in Fig.1.

The hot compression tests were performed using a Gleeble-3800 thermal simulator in a deformation temperature range of 250–400 ℃ and strain rate range of 0.001–1 s^{-1}. According to the schematic diagram of hot deformation in Fig.1b, the samples were firstly heated to the preset temperature at a heating rate of 5 ℃/s and held at this temperature for 5–10 min before hot compression testing. Graphite mixed with grease was used at both ends of samples as the lubricant. All samples were deformed up to a true strain of about 70% and quenched in water.

Phase analysis of the alloys was conducted using a Rigaku D/max2500PC X-ray diffractometer (XRD) with a scanning angle ranging from 10° to 90° and a scanning rate of 4 °/min. Scanning electron microscope (SEM, JEOL JSM-7800F), transmission electron microscope (TEM, FEI Tecnai G2 F20), and electron backscattered diffractometer (EBSD) were used for microstructure analyses.

Table 1 Measured composition of ZM61-0.5Ca and ZMT612-0.5Ca alloys (wt%)

Alloy	Zn	Mn	Sn	Ca	Mg
ZM61-0.5Ca	5.93	0.73	-	0.58	Bal.
ZMT612-0.5Ca	6.02	0.58	2.05	0.53	Bal.

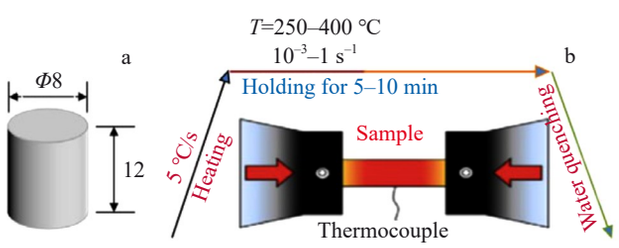

Fig.1 Dimensional drawing of hot compression sample (a) and schematic diagram of hot compression test (b)

3 Results and Discussion

3.1 Microstructure analysis

XRD patterns and corresponding phase analysis results of homogenized alloys are shown in Fig.2. The diffraction peaks corresponding to the $Ca_2Mg_6Zn_3$ and Mg-Zn phases can still be detected in ZM61-0.5Ca alloy. With the addition of Sn, the diffraction peaks of CaMgSn phase appear. Fig.3 shows SEM images of the microstructure of the as-cast and homogenized alloys. The continuous eutectic phases of as-cast ZM61-0.5Ca alloy mainly consist of $Ca_2Mg_6Zn_3$ and Mg-Zn phases, which are mostly distributed along the grain boundaries. With the addition of Sn, these continuous phases are broken and refined, and feather-like CaMgSn intermetallic compounds appear, which are mainly distributed in the matrix or near grain boundaries. After homogenization, some eutectic phases are dissolved and diffused into the matrix, as shown by the dotted circles in Fig. 3c and 3d. It indicates that most of the Mg-Zn phases and some $Ca_2Mg_6Zn_3$ phases can dissolve into *α*-Mg, while almost all CaMgSn phases remain undissolved even after the homogenization treatment.

EBSD analyses of the two alloys at a strain rate of 0.001 s^{-1} are shown in Fig. 4. Inverse pole figures (IPFs) of the two alloys are shown in Fig.4a–4d. At a deformation temperature of 250 ℃, fine recrystallized grains are found along the grain boundaries, suggesting that dynamic recrystallization (DRX) has occurred but is not fully completed. When the temperature rises up to 350 ℃, however, equiaxed microstructures are presented, as shown in Fig. 4c – 4d, indicating a significant

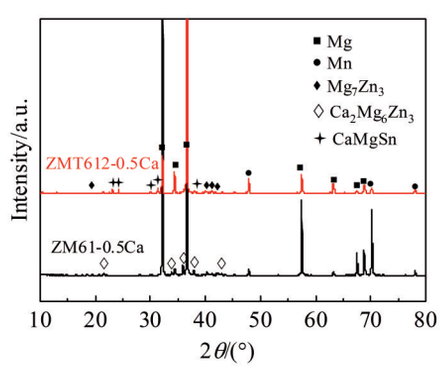

Fig.2 XRD patterns of homogenized ZM61-0.5Ca and ZMT612-0.5Ca alloys

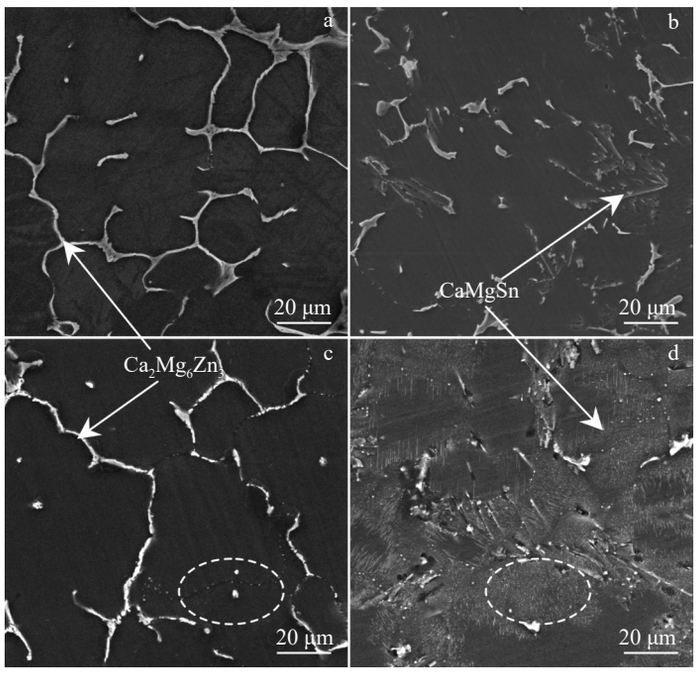

Fig.3 SEM images of as-cast (a–b) and homogenized (c–d) ZM61-0.5Ca alloy (a, c) and ZMT612-0.5Ca alloy (b, d)

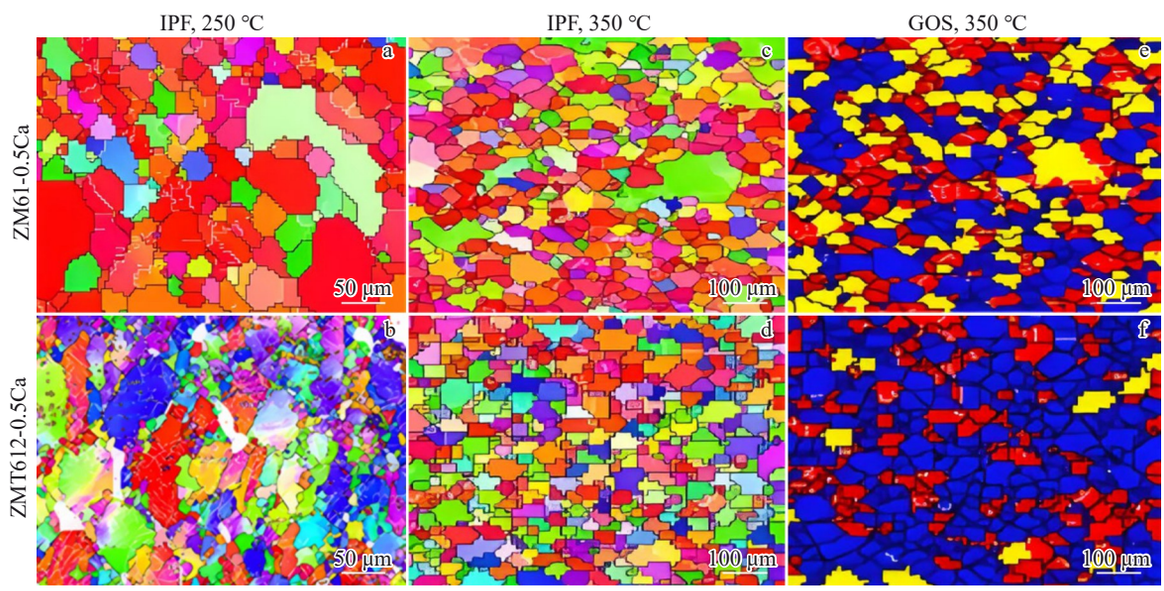

Fig.4 IPF (a–d) and GOS maps (e–f) of ZM61-0.5Ca alloy (a, c, e) and ZMT612-0.5Ca alloy (b, d, f) at strain rate of 0.001 s^{-1} and deformation temperatures of 250 and 350 °C

enhancement in DRX extent. According to grain orientation spread (GOS) maps obtained at 350 °C (Fig. 4e – 4f), the recrystallized fraction increases from 43% to 74% with the addition of Sn. The reason is that the residual CaMgSn phases can act as nucleation sites during deformation. Feather-like CaMgSn phases can increase the energy storage and promote the recrystallization nucleation in the deformation zone with Sn addition[16]. In addition, the average grain sizes of ZM61-0.5Ca and ZMT612-0.5Ca alloys at 350 °C are about 36 and 28 μm, respectively, which reveals that grain growth can be hindered by addition of Sn. TEM micrographs of the deformed alloys (tested at 350 °C and a strain rate $\dot{\varepsilon}$ of 0.001 s^{-1}) are shown in Fig.5. Due to high thermal stability of $Ca_2Mg_6Zn_3$ and CaMgSn phases, these particles of a high density remain in the microstructure even after hot deformation at 350 °C. Recrystallized grains are found along grain boundaries for both alloys. It can also be seen that Sn addition leads to the formation of fine grains with wavy grain boundaries, which is a typical microstructural feature of DRX-induced grain refinement, as reported in Ref.[17].

3.2 Flow stress behavior

The flow true stress-true strain curves of alloys under different hot deformation conditions are shown in Fig. 6. It shows that both alloys have obvious DRX characteristics. At

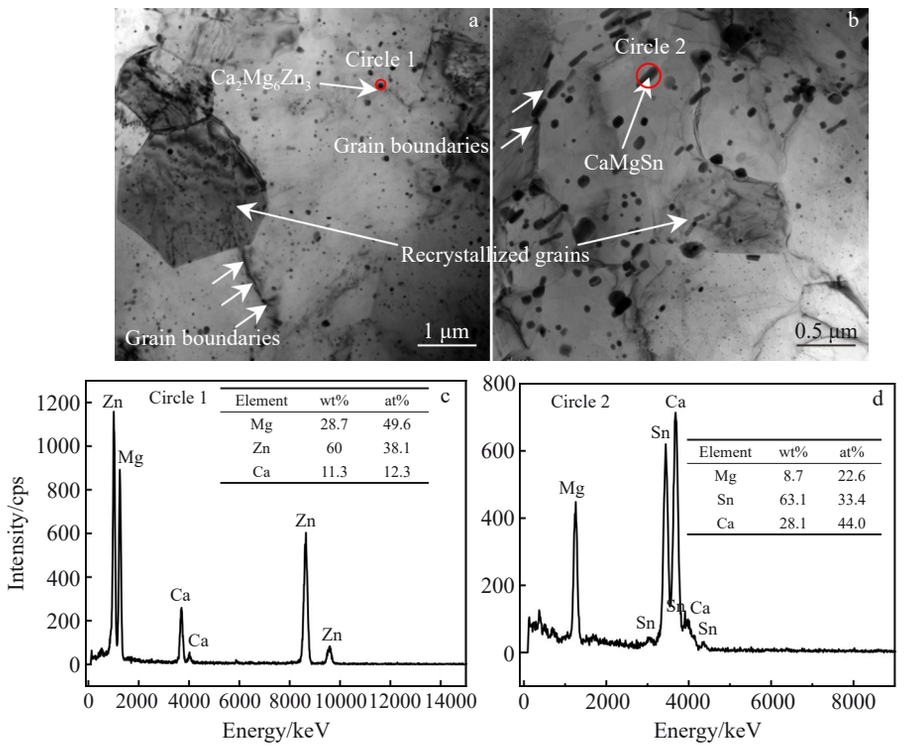

Fig.5 TEM images (a–b) and EDS results (c–d) of deformed alloys at 350 °C and 0.001 s^{-1}: (a, c) ZM61-0.5Ca alloy and (b, d) ZMT612-0.5Ca alloy

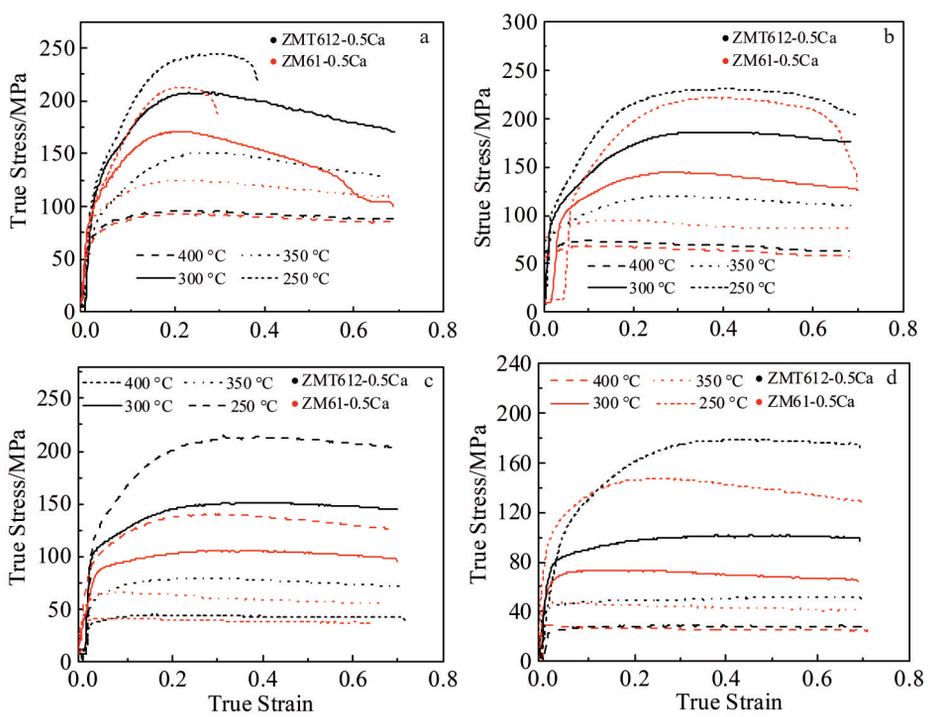

Fig.6 Flow true stress-true strain curves of ZMT612-0.5Ca and ZM61-0.5Ca alloys under different deformation conditions: (a) $\dot{\varepsilon}$=1 s^{-1}, (b) $\dot{\varepsilon}$=0.1 s^{-1}, (c) $\dot{\varepsilon}$=0.01 s^{-1}, and (d) $\dot{\varepsilon}$=0.001 s^{-1}

lower deformation temperatures or higher strain rates, the true stress-true strain curves can be divided into two stages, including work hardening and dynamic softening, with an obvious peak stress. It is well known that thermal deformation is influenced by work hardening and dynamic softening effects[21]. In the work hardening stage, dislocations accumulate and entangle with each other, which leads to an increase in flow stress with increasing the strain. Once the peak stress is reached, dynamic softening is dominant. However, at higher deformation temperature or lower strain

rate, a steady-state flow stress appears in an early deformation stage without visible peak stress which is in good agreement with findings of earlier studies[18–20]. As the deformation temperature increases, dynamic recovery (DRV) and DRX are easier to occur. Therefore, the true stress-true strain curve exhibits flow softening at lower strains, followed by a steady-state flow region.

As shown in Fig. 6a, under the deformation condition of 250 ℃ and 1 s^{-1}, the flow stress of both ZM61-0.5Ca and ZMT612-0.5Ca alloys drops rapidly during the final deformation stage due to fracture. At low temperatures, non-basal slip systems are more difficult to be activated compared with those at higher temperatures. Additionally, the effective time for dislocation slip and climb is shortened under higher strain rates. Consequently, dynamic softening effect is hindered, while work hardening effect is obvious in the early deformation stage. Failure also occurs for ZM61-0.5Ca alloy at 250 ℃ and a strain rate of 0.1 s^{-1}, as shown in Fig.6b, but this phenomenon does not happen for ZMT612-0.5Ca alloy. It indicates that the addition of Sn can improve the deformation capacity of the alloy. According to our previous research[13], the intensity of basal texture in dynamically recrystallized regions decreases with the addition of Sn, resulting in easier activation of non-basal slip systems. Moreover, the grains are refined with the addition of Sn.

The peak stress is usually an important factor during deformation, and the peak stress values of the two alloys are summarized in Fig. 7. It can be seen that the deformation temperature and strain rate have obvious influences on the peak stress. In general, the peak stress decreases with increasing the temperature at a constant strain rate; besides, peak stress increases with the increasing strain rate at a certain deformation temperature.

It is generally believed that the thermal activation of atoms and the mobility of dislocations are enhanced when the temperature increases, and more dislocations can slip and climb during deformation, thereby rendering the softening effect prominent[22] and consequently reducing the peak stress. In addition, the CRSS on non-basal planes decreases significantly with the increase in deformation temperature for Mg alloys[23], thus decreasing the peak stress. In contrast, when the strain rate increases, the time available for deformation under a given strain is shortened, and the dislocation movement is blocked, so the work hardening effect is dominant, which leads to the increase in flow stress.

Under the same deformation temperature and strain rate, the peak stress of ZMT612-0.5Ca alloy is consistently higher than that of ZM61-0.5Ca alloy. The reasons for this improved stress include grain refinement and second-phase strengthening; specifically, the needle-like CaMgSn phase can effectively inhibit dislocation motion.

3.3 Constitutive equation

According to the Arrhenius equations[24–26], the relationship between deformation temperature (T), strain rate ($\dot{\varepsilon}$), and flow stress(σ) under different deformation conditions can be described as follows:

$$\dot{\varepsilon} = A_1 \sigma^{n_1} \exp(-Q/RT) \quad (\alpha\sigma \leqslant 0.8) \tag{1}$$

$$\dot{\varepsilon} = A_2 \exp(\beta\sigma) \exp(-Q/RT) \quad (\alpha\sigma \geqslant 1.2) \tag{2}$$

$$\dot{\varepsilon} = A[\sinh(\alpha\sigma)]^n \exp(-Q/RT) \text{ (for all } \sigma) \tag{3}$$

where Q is the deformation activation energy; T is temperature; A_1, A_2, A, α, β, n_1 with n are material constants with $\alpha=\beta/n_1$; R is the mole gas constant of 8.314 J·(mol·K)$^{-1}$.

The n_1 and β can be obtained by $n_1=(\partial \ln\varepsilon)/\partial \ln\sigma$ and $\beta=(\partial \ln\varepsilon)/\partial\sigma$. Fig. 8 illustrates the linear relationships of $\ln\sigma_P$-$\ln\dot{\varepsilon}$ and σ_P-$\ln\dot{\varepsilon}$ for ZM61-0.5Ca and ZMT612-0.5Ca alloys at different deformation temperatures. Based on Fig.8, the values of n_1 and β can be obtained as follows: for the ZM61-0.5Ca alloy, n_1=7.99 and β=0.103; for the ZMT612-0.5Ca alloy, n_1=16.03 and β=0.109. Thus, α values are calculated to be 0.0129 for ZM61-0.5Ca alloy and 0.0074 for ZMT612-0.5Ca alloy.

Fig.9 presents the linear relationships of $\ln[\sinh(\alpha\sigma)]$-$\ln\dot{\varepsilon}$ at different deformation temperatures and $\ln[\sinh(\alpha\sigma)]$-1000/T at different strain rates for ZM61-0.5Ca and ZMT612-0.5Ca alloys. Therefore, the values of n and Q can be obtained as follows: n=5.85 and Q=199.654 kJ/mol for ZM61-0.5Ca alloy; n=7.53 and Q=276.649 kJ/mol for ZMT612-0.5Ca alloy.

In addition, the combined effect of deformation temperature and strain rate can be described by the Zener-Hollomon parameter (Z), as follows[27–28]:

$$Z = \dot{\varepsilon} \exp(Q/RT) = A[\sinh(\alpha\sigma)]^n \tag{4}$$

Fig. 10 depicts the fitting lines in $\ln Z$-$\ln[\sinh(\alpha\sigma)]$ plots, indicating a good linear relationship between $\ln Z$ and $\ln[\sinh(\alpha\sigma)]$ for ZM61-0.5Ca and ZMT612-0.5Ca alloys.

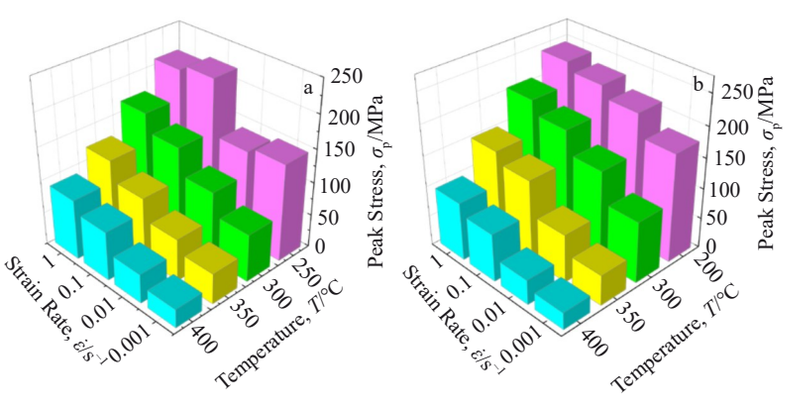

Fig.7 Peak stress of ZM61-0.5Ca (a) and ZMT612-0.5Ca (b) alloys

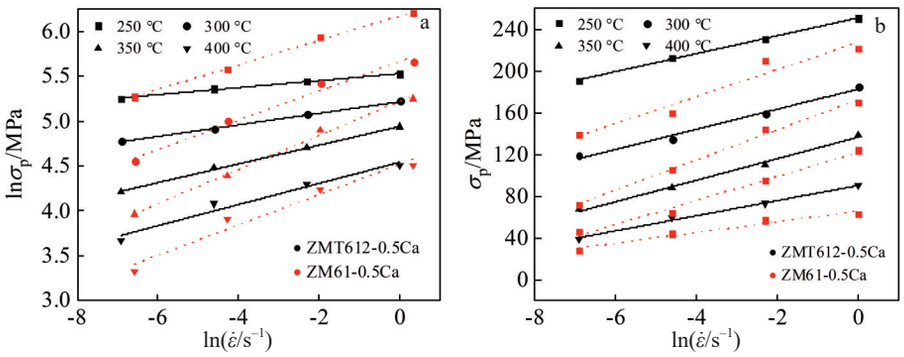

Fig.8 Relationships of $\ln\sigma_p$-$\ln\dot{\varepsilon}$ (a) and σ_p-$\ln\dot{\varepsilon}$ (b) for ZM61-0.5Ca and ZMT612-0.5Ca alloys

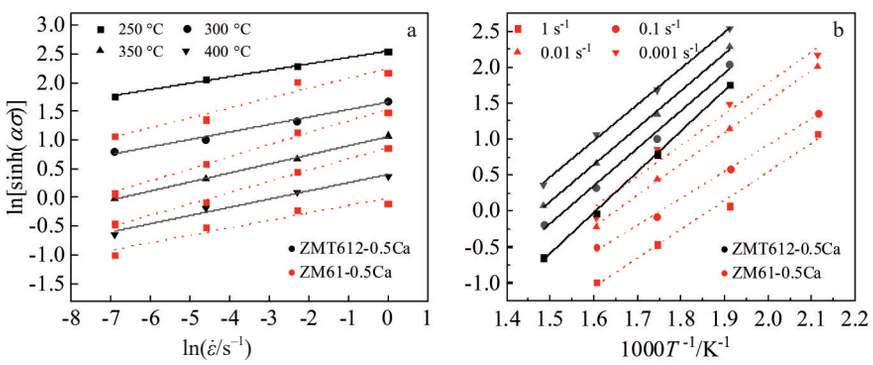

Fig.9 Relationships of $\ln[\sinh(\alpha\sigma)]$-$\ln\dot{\varepsilon}$ (a) and $\ln[\sinh(\alpha\sigma)]$-$1000/T$ (b) for ZM61-0.5Ca and ZMT612-0.5Ca alloys

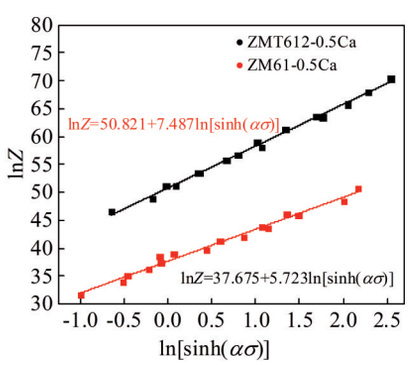

Fig.10 Relations between $\ln Z$ and $\ln[\sinh(\alpha\sigma)]$ for ZM61-0.5Ca and ZMT612-0.5Ca alloys

Thus, the values of $\ln A$ can be obtained by linear regression analysis in Fig.10. Therefore, the value of A can be calculated: $A=2.302\times10^{16}$ for ZM61-0.5Ca alloy and $A=1.178\times10^{22}$ for ZMT612-0.5Ca alloy.

Finally, the values of various parameters of the two alloys are put into Eq. (3), and the constitutive relations for ZM61-0.5Ca and ZMT612-0.5Ca alloys are established as follows:

$$\dot{\varepsilon}=2.302\times10^{16}[\sinh(0.0129\sigma)]^{5.85}\exp\left(\frac{-199.654\times10^{3}}{8.314T}\right) \quad (5)$$

$$\dot{\varepsilon}=1.178\times10^{22}[\sinh(0.0074\sigma)]^{7.53}\exp\left(\frac{-276.649\times10^{3}}{8.314T}\right) \quad (6)$$

According to Eq.(4), the peak flow stress can be expressed by the Zener-Hollomon parameter Z, as follows:

$$\sigma=\frac{1}{0.0129}\left\{\left(\frac{Z}{2.302\times10^{16}}\right)^{1/5.58}+\left[\left(\frac{Z}{2.302\times10^{16}}\right)^{2/5.85}+1\right]^{1/2}\right\} \quad (7)$$

$$\sigma=\frac{1}{0.0074}\left\{\left(\frac{Z}{1.178\times10^{22}}\right)^{1/7.53}+\left[\left(\frac{Z}{1.178\times10^{22}}\right)^{2/7.53}+1\right]^{1/2}\right\} \quad (8)$$

Table 2 lists all parameters of ZM61-0.5Ca and ZMT612-0.5Ca alloys in their respective constitutive equations. The values of n, Q, and A for ZM61-0.5Ca alloy are lower than those for ZMT612-0.5Ca alloy, while the value of α exhibits an opposite trend. It is known that Q, defined as the activation energy of deformation, represents the energy threshold required for deformation. Obviously, the Q values of two alloys are both higher than the activation energy of lattice self-diffusion (135 kJ/mol) [29] and grain boundary diffusion (92 kJ/mol) [30] of pure Mg, indicating that there is an additional mechanism except the simple diffusion in these alloys. The sufficient energy is required to overcome the energy barrier for the cross-slip of screw dislocations from basal planes to prismatic planes. In addition, the Q value of ZM61-0.5Ca alloy is relatively higher than that of the ZM51[31] and ZM61[29] alloys. Adding 2wt% Sn to ZM61-0.5Ca increases the Q value from 199.65 kJ/mol to 276.65 kJ/mol,

Table 2 Parameters in constitutive equations of ZM61-0.5Ca and ZMT612-0.5Ca alloys

Alloy	α	n	Q/kJ·mol^{-1}	A
ZM61-0.5Ca	0.0129	5.85	199.654	2.302×10^{16}
ZMT612-0.5Ca	0.0074	7.53	276.649	1.178×10^{22}

thus enhancing the thermal stability of ZMT612-0.5Ca alloy. Higher values of Q should be attributed to the formation of CaMgSn particles (as shown in Fig. 5), which may provide obstacles to dislocation movement, leading to more energy required for dislocation cross-slip or climbing.

3.4 Processing maps

Prasad[33] and Sivakesavam[34] et al developed processing maps based on the dynamic materials mode (DMM) [32] to predict the hot deformation behavior of various materials and to optimize their hot processing parameters. According to Prasad's theory, the total external power (P) absorbed by a material during hot deformation usually can be divided into two parts: the dissipative energy (G) and the structural transformation energy (J). G is used for dislocation motion, and J is used for microstructure evolutions. The relationship among P, G, and J is expressed as follows[35]:

$$P = G + J = \sigma\dot{\varepsilon} = \int_0^{\dot{\varepsilon}} \sigma \mathrm{d}\dot{\varepsilon} + \int_0^{\sigma} \dot{\varepsilon} \mathrm{d}\sigma \tag{9}$$

where σ is the true tress (MPa) and $\dot{\varepsilon}$ is the strain rate. The strain rate sensitivity parameter m, which has huge influences on G and J, can be obtained by Eq.(10):

$$m = \frac{\mathrm{d}J}{\mathrm{d}G} = \frac{\dot{\varepsilon}\mathrm{d}\sigma}{\sigma\mathrm{d}\dot{\varepsilon}} = \frac{\mathrm{d}\ln\sigma}{\mathrm{d}\ln\dot{\varepsilon}} \tag{10}$$

The efficiency of power dissipation (η) can be represented by:

$$\eta = \frac{2m}{m+1} \tag{11}$$

The power dissipation contour map is constituted by the efficiency of power dissipation (η) associated with deformation temperature (T) and deformation rate ($\dot{\varepsilon}$). Besides, instability criterion (ξ) is usually used to describe flow instability of materials at a certain deformation temperature and a certain deformation rate, which can be given by:

$$\xi(\dot{\varepsilon}) = \frac{\partial \ln(m/m+1)}{\partial(\ln\dot{\varepsilon})} + m < 0 \tag{12}$$

The rheological instability contour map is composed by instability criterion (ξ) as a function of deformation temperature (T) and deformation rate ($\dot{\varepsilon}$). The processing maps can be obtained by superimposing the power dissipation contour map onto the rheological instability contour.

Fig. 11 shows the processing maps of ZM61-0.5Ca and ZMT612-0.5Ca alloys developed at a strain range of 0.1–0.3. As indicated, the efficiency value is elevated with the increase in deformation temperature or the decrease in strain rate. The shaded parts represent the instability region while the red-circled regions represent the safe hot working regions.

The rheological instability regions (unsafe regions) are mainly concentrated at high strain rates in the initial deformation stage. When the true strain reaches 0.3, the area of instability zone of the two alloys becomes larger. It is well known that Mg alloys have low stacking fault energy (SFE) and DRX process is the main softening mechanism during hot deformation[36]. The threshold value of power dissipation efficiency required to trigger DRX is generally recognized to be 0.3 for Mg alloys[37].

As shown in Fig. 11a – 11c, the optimal hot working parameters of ZM61-0.5Ca alloy vary slightly with true strain. At a true strain of 0.1, the optimal conditions are achieved at a

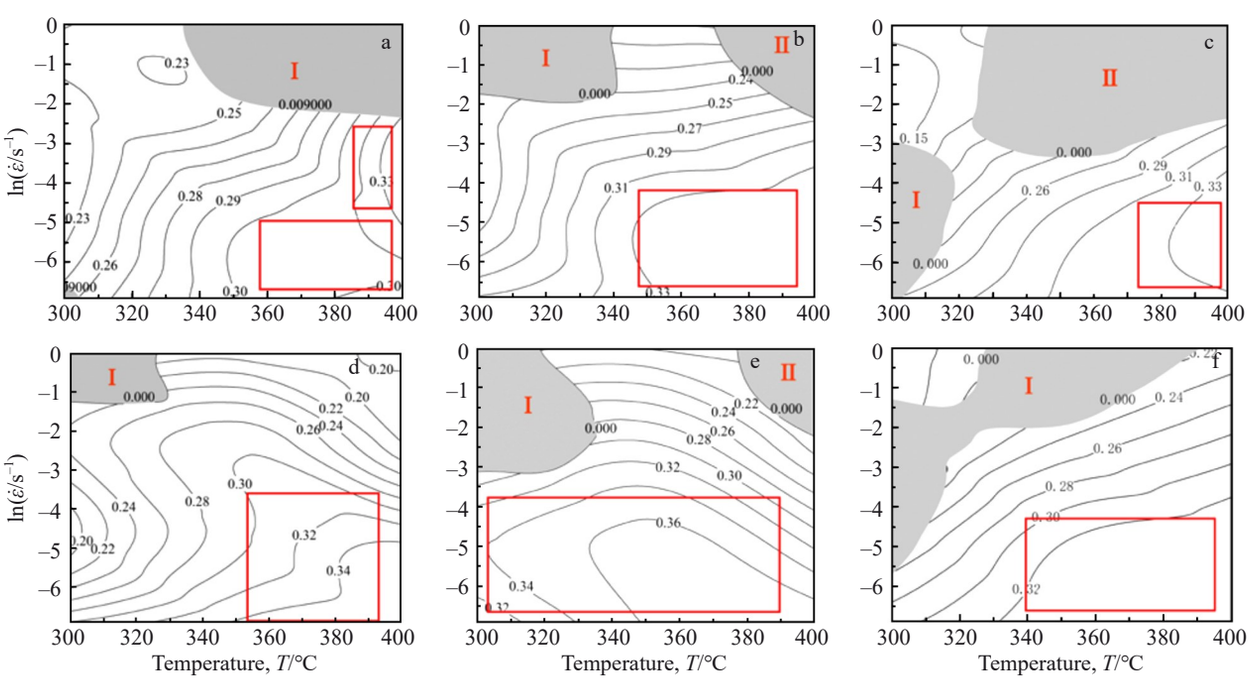

Fig.11 Processing maps of ZM61-0.5Ca (a–c) and ZMT612-0.5Ca (d–f) alloys at different true strains: (a, d) 0.1, (b, e) 0.2, and (c, f) 0.3

deformation temperature of 350–400 ℃ with a strain rate of 0.001–0.005 s^{-1}, or alternatively at a deformation temperature of 380–400 ℃ with a strain rate of 0.005–0.05 s^{-1}. When the true strain is 0.2, the optimal processing is achieved at a deformation temperature of 350–400 ℃ with strain rate of 0.001–0.01 s^{-1}. When the strain is 0.3, optimal processing occurs at a deformation temperature of 370–400 ℃ with a strain rate of 0.001–0.005 s^{-1}.

As shown in Fig. 11d – 11f, the optimal hot working parameters for the ZMT612-0.5Ca alloy vary with true strain, and the specific conditions are summarized as follows. At a true strain of 0.1, optimal deformation is achieved at a deformation temperature of 350–400 ℃ with a strain rate of 0.001–0.01 s^{-1}. When the strain is 0.2, the optimal processing window expands to a deformation temperature of 300–400 ℃ while maintaining a strain rate of 0.001–0.01 s^{-1}. When the strain is 0.3, the optimal conditions shift to a deformation temperature of 340–400 ℃ and a strain rate of 0.001–0.005 s^{-1}.

It can be deduced that the optimal hot working parameters for the ZM61-0.5Ca alloy are a deformation temperature range of 380–400 ℃ and a strain rate range of 0.001–0.005 s^{-1}. For the ZMT612-0.5Ca alloy, the optimal hot working parameters correspond to a deformation temperature range of 350–400 ℃ and a strain rate range of 0.001–0.01 s^{-1}. The addition of Sn effectively expands the hot working window of the ZM61-0.5Ca alloy.

4 Conclusions

1) Residual CaMgSn phases act as nucleation sites for DRX during compression deformation, thus promoting the DRX process. Grain growth with the increase in temperature is hindered with Sn addition.

2) The ZM61-0.5Ca and ZMT612-0.5Ca alloys exhibit distinct DRX characteristics, and their hot deformation processes are jointly influenced by work hardening and dynamic softening effects. Short rod-like CaMgSn phases formed in the Sn-containing alloy (ZMT612-0.5Ca) can effectively inhibit dislocation motion, thus increasing the peak flow stress of the alloy compared to that of the Sn-free ZM61-0.5Ca alloy.

3) The hot deformation activation energies of ZM61-0.5Ca and ZMT612-0.5Ca alloys are determined to be 199.654 and 276.649 kJ/mol, respectively. The addition of Sn increases the hot deformation activation energy of the ZM61-0.5Ca alloy, thus improving the thermal stability of the alloy during hot working.

4) The optimal hot deformation parameters for the ZMT612-0.5Ca alloy are identified as a deformation temperature range of 350–400 ℃ and a strain rate range of 0.001–0.01 s^{-1}.

References

1 He R H, Wang H, Zhang Z *et al. Rare Metal Materials and Engineering*[J], 2023, 52(11): 3697

2 Chen X , Zhang D F , Zhao Y *et al. Journal of Materials Research and Technology*[J], 2022, 17: 925

3 Pan H C, Ren Y P, Fu H *et al. Journal of Alloys and Compounds*[J], 2016, 663: 321

4 Clark J B. *Acta Metallurgica*[J], 1965, 13(12): 1281

5 Qi F G, Zhang D F, Zhang X H *et al. Journal of Alloys and Compounds*[J], 2014, 585: 656

6 Naghdi F, Mahmudi R, Kang J Y *et al. Materials Science and Engineering A*[J], 2016, 649: 441

7 Du Y Z, Qiao X G, Zheng M Y *et al. Materials & Design*[J], 2016, 98: 285

8 Du Y Z, Zheng M Y, Jiang B L. *Journal of Materials Research*[J], 2018, 33(8): 1003

9 Zhang B P, Wang Y, Geng L *et al. Materials Science and Engineering A*[J], 2012, 539: 56

10 Zhang Y, Song L P, Chen X Y *et al. Materials*[J], 2018, 11(9): 1490

11 Jardim P M, Solorzano G, Vander S J B. *Materials Science and Engineering A*[J], 2004, 381(1–2): 196

12 Pan H C, Qin G W, Xu M *et al. Materials & Design*[J], 2015, 83: 736

13 Chen X, Zhang D F, Xu J Y *et al. Journal of Alloys and Compounds*[J], 2021, 850: 156711

14 Chen X, Zhang D F, Feng J K *et al. Rare Metal Materials and Engineering*[J], 2020, 49(9): 2920

15 Chalasani D, Kamineni R, Kalidass S *et al. Metals*[J], 2018, 8(4):216

16 Jia Y Y, Cai Z H, Fan Q H *et al. Transactions of the Indian Institute of Metals*[J], 2022, 75(7): 1751

17 Srinivasan M, Loganathan C, Narayanasamy R *et al. Materials & Design*[J], 2013, 47: 449

18 Wu H, Wen S P, Huang H *et al. Materials Science and Engineering A*[J], 2016, 651: 415

19 Wang B J, Zhang Y, Tian B H *et al. Vacuum*[J], 2018, 155: 594

20 Hui Y U, Yu H, Kim Y *et al. Transactions of Nonferrous Metals Society of China*[J], 2013, 23(3): 756

21 Zhi C C, Wu Z Y, Lei J Y *et al. Metals*[J], 2023, 13(4): 645

22 Zhang Q, Li Q A, Chen X Y *et al. Materials Science and Engineering A*[J], 2021, 826:142026

23 Galiyev A, Kaibyshev R, Gottstein G. *Acta Materialia*[J], 2001, 49(7): 1199

24 Chen X R, Liao Q Y, Niu Y X *et al. Journal of Alloys and Compounds*[J], 2019, 803: 585

25 Jeong H T, Han S H, Kim W J. *Journal of Alloys and Compounds*[J], 2019, 788: 1282

26 Zhao J W, Ding H, Zhao W J *et al. Computational Materials Science*[J], 2014, 92: 47

27 Somekawa H, Hirai K, Watanabe H *et al. Materials Science and Engineering A*[J], 2005, 407(1–2): 53

28 Cheng W, Tian Q W, Yu H *et al. Materials & Design*[J], 2015, 85: 762

29 Peng Jian, Tong Xiaoshan, Shang Shouliang *et al. Rare Metal*

Materials and Engineering[J], 2013, 42(8):1627 (in Chinese)
30 Wang C, Liu Y T, Lin T *et al. Materials Characterization*[J], 2019, 157: 109896
31 Mu T, Zhang K, Li Y J *et al. Journal of Materials Research and Technology*[J], 2023, 22: 838
32 Yao J J, Zhang D, Zhang J S. *Rare Metal Materials and Engineering*[J], 2022, 51(6): 2046
33 Prasad Y, Seshacharyulu T. *Materials Science and Engineering A*[J], 1998, 243(1–2): 82
34 Sivakesavam O, Prasad Y. *Materials Science and Engineering A*[J], 2002, 323(1–2): 270
35 Ghosh A, Elasheri A, Parson N *et al. Journal of Alloys and Metallurgical Systems*[J], 2024, 6: 100077
36 Cho C H, Son K T, Lee J C *et al. Materials Science and Engineering A*[J], 2020, 786: 139471
37 An D, Qian B Y, Wu R Z *et al. Journal of Rare Earths*[J], 2024, 12(42): 2341

Mg-Zn-Mn(-Sn)-Ca合金的热压缩变形行为及加工图

陈　霞[1]，朱禹龙[1]，刘全义[1]，张丁非[2]，潘复生[2]
(1. 中国民航飞行学院 民航安全工程学院，四川 广汉 618307)
(2. 重庆大学 材料科学与工程学院，重庆 400045)

摘　要：研究了Mg-6Zn-1Mn-0.5Ca（ZM61-0.5Ca）和Mg-6Zn-1Mn-2Sn-0.5Ca（ZMT612-0.5Ca）合金在250~400 ℃和0.001~1 s^{-1}条件下的热压缩变形行为。结果表明：添加Sn促进了动态再结晶，CaMgSn相可作为压缩变形过程中的形核位点。流变应力随应变速率的增加和温度的降低而增大。ZM61-0.5Ca和ZMT612-0.5Ca合金具有明显的动态再结晶特征。加入Sn后，CaMgSn相能有效抑制位错运动，从而提高合金的峰值流变应力。Sn的加入使ZM61-0.5Ca合金的热变形活化能从199.654 kJ/mol提高到276.649 kJ/mol，提高了合金的热稳定性。ZMT612-0.5Ca合金的最佳热变形参数为变形温度350~400 ℃、应变速率0.001~0.01 s^{-1}。

关键词：热变形；本构方程；加工图；变形激活能；镁合金

作者简介：陈 霞，女，1990年生，博士，中国民航飞行学院民航安全工程学院， 四川 广汉 618307，E-mail：chenxia13091025@163.com